Highly oriented NiSi$_2$@Si thin-nanocomposite produced by solid state diffusion: Morphological and crystallographic characterization

Daniel da Silva Costa [a], Guinther Kellermann [a,*], Aldo F. Craievich [b], Luciano A. Montoro [c], Camilla K.B.Q.M. Oliveira [a], Conrado R.M. Afonso [d], Cristián Huck-Iriart [e], Lisando J. Giovanetti [f], Felix G. Requejo [f], Igor G. Zanella [g], Irineu Mazzaro [a], Erico S. Szameitat [a], Rodrigo P. Cardoso [g]

[a] *Department of Physics, University Federal of Paraná, mailbox 19091, Curitiba, Paraná 81531-990, Brazil*
[b] *Institute of Physics, University of Sao Paulo, CP 66318, CEP 05315-970, São Paulo, Brazil*
[c] *Department of Chemistry, University Federal of Minas Gerais, Belo Horizonte, Minas Gerais, Brazil*
[d] *University Federal of São Carlos, São Carlos, São Paulo, Brazil*
[e] *Escuela de Ciencia y Tecnología, Universidad Nacional de San Martín (UNSAM), Campus Miguelete, 25 de Mayo y Francia, San Martín, Provincia de Buenos Aires 1650, Argentina*
[f] *Instituto de Investigaciones Fisicoquímicas Teóricas y Aplicadas (INIFTA, National University of La Plata (UNLP) and CONICET, CC/16 suc. 4, La Plata 1900, Argentina*
[g] *Department of Mechanical Engineering, University Federal of Paraná, Curitiba, Paraná, Brazil*

ARTICLE INFO

ABSTRACT

This article describes a morphological and crystallographic multi-technique characterization of a 2D-nanocomposite consisting of highly oriented NiSi$_2$ nanoplates endotaxially grown inside a single-crystalline Si(001) wafer close to its external surface. This nanostructured material is prepared using a novel procedure which promotes the diffusion of Ni atoms from a deposited Ni-dopped-SiO$_2$ thin film into the volume of a Si(001) flat wafer under controlled thermodynamic conditions. High Resolution Scanning Transmission Electron Microscopy images reveal the formations of well oriented thin hexagonal nanoplates totally buried inside a Si(001) wafer and randomly oriented nearly spherical Ni nanocrystals located inside the Ni-doped SiO$_2$ thin film and also inside a thin layer close to external surface of the Si(001) wafer. The NiSi$_2$ nanoplates formed by endotaxial growth have their large hexagonal flat surfaces parallel to one of the four Si{111} crystallographic planes and exhibit coherent 7A-type interfaces with the host Si matrix. Additional analyses of Grazing-Incidence Small-Angle X-ray Scattering patterns - which probe a high number of nanoparticles - indicated that the average thickness and maximum diameter of NiSi$_2$ nanoplates are 12 nm and 118 nm, respectively, and the average radius of Ni nanocrystals is 1.7 nm. The described process for obtaining 2D-NiSi$_2$@Si nanocomposites opens new possibilities for exploiting the structural features of these materials for use in devices requiring anisotropic electrical transport properties.

1. Introduction

Transition metal silicides based nanocomposites which include CoSi$_2$, TiSi$_2$, NiSi and NiSi$_2$ have attracted attention in recent decades due to their specific electrical features [1,2]. Since NiSi$_2$ and CoSi$_2$ exhibit high electrical conductivity and thermal stability, they are usually employed as contact material in microelectronics [2–8]. Moreover, higher-level hierarchical nanocomposites with ordering substructure would be a novel direction in the development of new thermoelectric materials, sensors and energy storage devices [9–12]. Different synthesis methods were described in the literature for promoting the epitaxial or endotaxial growth of metal silicide structures with defined or undefined shapes [9,13–17]. These nanostructures have different shapes depending on the synthesis methods and formation process [9,13–16,18,19].

Previous works described the property of transition metal atoms which selectively diffuse along particular crystallographic planes in single-crystalline silicon wafers and leads to the endotaxial formation of metal silicide nanoparticles with high aspect ratio shapes, such as wires,

---

pyramid-like and thin plates. These structures are usually obtained under very high vacuum and high temperature conditions by evaporation and deposition of low quantities of the metal for avoiding metal cluster aggregation [20].

In a previews work, the formation of highly oriented arrays of CoSi$_2$ nanoplates endotaxially grown in single-crystalline Si wafers was described [21]. These nanostructures were obtained through solid/solid thermal diffusion at room pressure from a deposited Co-doped SiO$_2$ thin film to a single-crystalline Si wafer. In this case, the precursor solution of the Co-doped thin film was deposited in a single step on silicon wafer without removal of the native oxide. The CoSi$_2$ nanoplates exhibit a nearly regular hexagonal shape and - irrespective of the crystallographic orientation of the surface of the Si wafer - they grow with their large surfaces parallel to the lattice planes of the Si{111} crystallographic form [22] whose final size can be controlled by appropriate choice of temperature and thermal treatment time [23]. The mentioned previous works [21–23] dealt with the descriptions of the morphology, crystallographic structure, process kinetics and physicochemical aspects of the studied cobalt silicide (CoSi$_2$).

Besides CoSi$_2$, the nickel silicide NiSi$_2$ is widely used as a component of microelectronic and optoelectronic devices [24]. Because of the strong dependence of band alignment on the crystallographic orientation of the interface between NiSi$_2$ and the host silicon lattice, NiSi$_2$ nanocrystals in conjunction with the silicon matrix were also investigated in context of their use as Schottky barrier [25]. For this reason new preparation methods leading to NiSi$_2$ nanoparticles with desired shape and orientation are sought. Notice that the NiSi$_2$ nanoplates exhibit good electrical properties and their precursors are inexpensive and more environmentally friendly. Furthermore, the replacement of cobalt by nickel is desirable for green components.

We present in this study a structural and chemical characterization of a novel nanostructured material initially consisting of a Si(001) wafer in which a Ni-doped SiO$_2$-based thin film is deposited. The final nanostructured material that contains NiSi$_2$ nanoplates and Ni nanocrystals was prepared by a novel preparation method in which Ni is not directly deposited on Si wafer surface. Instead, the growth of the NiSi$_2$ nanoplates in Si is promoted by thermally activated diffusion of Ni atoms from the Ni-doped SiO$_2$ thin film deposited on the Si(001) wafer through the SiO$_2$:Si interface, thus allowing for a controlled chemical reaction with Si atoms in the silicon wafer. The endotaxial growth of NiSi$_2$ in the Si wafer is favored because the lattice parameter of NiSi$_2$ platelets is very close to the lattice parameter of the single-crystalline Si wafer.

Since the material studied here exhibit a complex nanostructure containing different types of nanoparticles, we decided to conduct our investigation by applying a multi-technique approach, including several imaging techniques such as atomic force microscopy (AFM), scanning transmission electron microscopy (STEM), energy-dispersive X-ray spectroscopy (XEDS) and also X-ray scattering techniques such as X-ray reflectometry (XRR) and grazing incidence small-angle X-ray scattering (GISAXS). Notice that imaging techniques in high-resolution mode provide useful insights on morphologic and crystallographic features of the nanoparticles over a rather small sample volume, while the scattering techniques yield global characterizations that probe a large volume and thus a much larger number of nanoparticles.

2. Material

A flat Si(001) wafer having a surface area of about 2×3 cm^2 was immersed in acetone and left under an ultrasonic bath for 10 min to remove organic residues. Subsequently, the wafer was embedded in a concentrated solution of HSO$_4$ acid (95%, Merck) and heated from room temperature up to 80 °C. The sample was then kept during 15 min at this temperature in order to remove any remaining organic contaminants. Removal of the native oxide layer from the silicon surface was achieved by immersion in a solution of HF acid (48%, Merck) for 1 min.

The precursor solution of a Ni-doped SiO$_2$-based gel was deposited

on the clean Si wafer immediately after etching. Finally, the thin film was formed by using the spin-coating procedure. Precursor solutions of the SiO$_2$-based thin film were deposited in two steps. The first step was a deposition of a solution of 0.15 g Ni(NO$_3$)$_2$·6H$_2$O (99.999%, Sigma-Aldrich) dissolved in 1.15 g isopropyl alcohol (98%, Merck) directly on the silicon substrate. The second step was a deposition of a precursor gel of the SiO$_2$ film on top of the first film. The precursor gel solution used in the second step contains 0.05 g of TEOS (tetraethyl orthosilicate, 99.999%, Sigma-Aldrich) and 0.30 g of aqueous solution of nitric acid (65% HNO$_3$, Merck) in 0.90 g of isopropyl alcohol (98%, Merck).

Prior to this two-step deposition procedure, the solution was kept at room temperature for one day, during which the hydrolysis reaction took place thus leading to the conversion of TEOS in SiO$_2$ and promoting the sol-gel transition [26–29]. During the deposition of the second gel solution, a re-dissolution of the first layer is expected to take place thus allowing for the diffusion of Ni^{2+} and NO$_3$$^-$ ions through the second gel layer. After having deposited 10 μL of each solution on the Si wafer, the samples were dried in air at room temperature thus allowing for a slow evaporation of volatiles. As a result, a deposited nanoporous dry SiO$_2$ thin film containing dispersed NiO species is obtained.

In order to promote the chemical reduction of Ni oxides embedded in the deposited thin film, the Si wafer and thin film were tentatively submitted to several isothermal treatments during 40 min over the 300–500 °C temperature range under a flow rate of 50 sccm in 5H$_2$+95He moisture at 1 atm. These isothermal treatments also lead to a partial compaction of the Ni-doped SiO$_2$ film and promotes the atomic diffusion of Ni atoms through the volume of the SiO$_2$ thin film and from the thin film - through the SiO$_2$:Si interface - into the silicon wafer. After further analyses of samples treated above 350 °C, we verified the formation of nanoparticles embedded in the SiO$_2$ thin film and also inside the Si wafer close to the Si:SiO$_2$ interface.

Instead of the one-step deposition procedure, the two-step procedure was chosen because the first deposition of Ni(NO$_3$)$_2$·6H$_2$O solution directly on the bare wafer increases the concentration of Ni species dispersed in the SiO$_2$ matrix in a layer close to silicon surface, thus favoring the diffusion of Ni into the Si wafer during the thermal treatment.

Furthermore, the preparation method described here differs from the procedure applied for the formation of CoSi$_2$ nanoplates in Si [21–23]. Notice that for the formation of CoSi$_2$ nanoplates the precursor solution of the thin film was deposited without removal of the native SiO$_2$ oxide. On the other hand, in our previous attempts to obtain endotaxial NiSi$_2$ nanoplates by deposition of the precursor solution on Si wafers without native oxide removal, the formation of NiSi$_2$ nanocrystals could not be achieved. This suggests that the native thin oxide layer on the Si wafer acts as a strong barrier for diffusion of Ni atoms.

GISAXS patterns from samples held above 350 °C showed the presence of a clear anisotropic contribution similar to that previously observed for the formation of CoSi$_2$ nanoplates [21–23]. This was our first experimental indication of the formation of NiSi$_2$ nanoplates in a Si (001) wafer, which, as it will be seen in next sections, was later clearly confirmed by high resolution imaging techniques. In this paper, samples consisting of Ni-doped SiO$_2$ thin films deposited on Si wafer, annealed during 40 min at 500 °C in H$_2$+He flow, were studied by AFM, STEM, XEDS, XRR, and GISAXS.

3. Experimental methods

Structural characterization by AFM was carried out using a Shimadzu SPM (SPM-9700) under intermittent (dynamic) mode. The measurements were conducted in air using standard silicon doped cantilevers with nominal spring constants k ~ 21–78 N/m and resonant frequency ω_0 ~ 250–390 kHz, with metallic reflex coating. All AFM images were processed (leveling, particle analysis) using the Shimadzu offline software.

STEM studies were performed using a double-corrected scanning transmission electron microscope FEI Titan Themis Cubed

(ThermoFisher Scientific) operating at 300 kV, equipped with Super-XEDS with four windowless silicon-drift detectors. High angle annular dark field (HAADF) images were acquired with collection angles between 66 and 200 mrad. STEM cross section specimens with surface perpendicular to the Si[110] zone axis were prepared using manual and dimpler polishing followed by Ar+ ion beam thinning with energies of 3.5 and 2 keV at incidence angles gradually decreasing from 6 to 2°.

GISAXS and XRR experiments were performed using a Discover D8 diffractometer from Bruker equipped with an X-ray microsource from Incoatec with a Cu target (X-ray wavelength λ = 0.15406 nm) together with a Montel multilayer focalization system. The full-width half-maximum diameter of the primary X-ray beam at the detection plane was equal to 0.5 mm. A Vantec 500 2D X-ray detector having a spatial resolution of 400 μm and a classical scintillation detector from Bruker were used to measure the GISAXS and XRR intensities, respectively.

In order to suppress absorption and scattering intensity from air, a vacuum path chamber was placed between the sample and the detector. The scattering intensity from a standard alumina sample was also recorded in order to precisely determine the sample-to-detector distance (333.2 mm) thus allowing us to determine the GISAXS intensity as a function of the X-ray scattering vector. The incidence angle between the direction of the primary X-ray beam α_i and the flat wafer surface was selected to be α_i=0.40 °. This value of α_i allowed us to probe the SiO_2 based thin film and the wafer volume in which $NiSi_2$ nanoplates are located while the minimum accessible wave-number for the measurements of GISAXS intensity became q_{min} = 0.33 nm^{-1}.

Fig. 1 shows a schematic view of the experimental setup used in the GISAXS experiment. The coordinates of each pixel of the detector were converted in coordinates of the scattering vector in reciprocal space using the relation:

$$\vec{q} = \frac{2\pi}{\lambda} \begin{pmatrix} \cos\alpha_f\cos2\theta_f - \cos\alpha_i \\ \cos\alpha_f\sin2\theta_f \\ \sin\alpha_f + \sin\alpha_i \end{pmatrix} \qquad (1)$$

where α_f is the angle between the direction of scattered beam and the sample surface and $2\theta_f$ is the angle between the projection of the scattered beam on xy plane and the x-axis. In Fig. 1 we also show the azimuthal angle ϕ that defines the orientation of the sample with respect to the axis normal to the sample surface. In our analysis we defined ϕ = 0 in case the projection of the direct beam on the sample surface is parallel to the Si[011] crystallographic direction. The parasitic scattering intensity - produced by windows, slits and air gaps between sample and vacuum paths - was subtracted from the total intensity. The full-width half-maximum of instrumental broadening function in y and
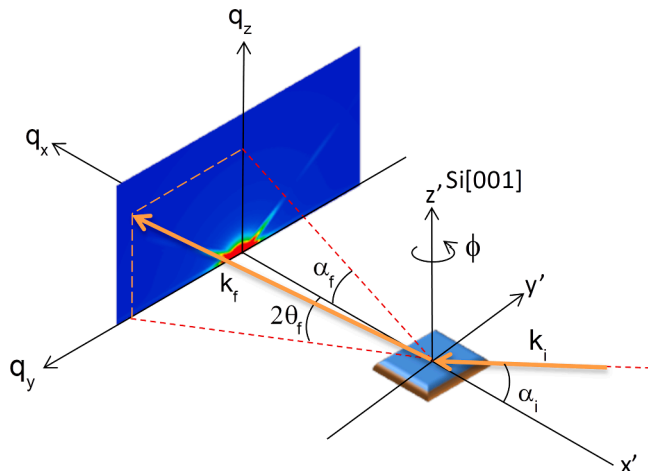
z-directions were $\Delta q_y = 0.12$ nm^{-1} and $\Delta q_z = 0.06$ nm^{-1}, respectively.

4. Experimental results

4.1. AFM and XRR

Our AFM results analyses are summarized in Fig. 2, which shows microscopy images of the surfaces of a Si wafer after being submitted to the successive preparation steps. The different images correspond to (i) a wafer covered by the native SiO_2 oxide after removal of organic compounds, (ii) the same wafer after etching, and (iii) the surface of the Ni-doped SiO_2 thin film after deposition on the Si wafer.

The AFM image displayed in Fig. 2(a) shows that after the first step of the preparation procedure, the surface of the native oxide on the Si wafers is essentially flat, with only weak scratches produced by the cutting and polishing tools. The image displayed in Fig. 2(b) shows that after the etching with HF acid the wafer surface becomes very rough and exhibits a grain-like structure with average radius ranging from 50 to 100 nm. Fig. 2(c) shows that the surface of the Ni-doped SiO_2 thin film is composed of a set of close-packed nanoparticles with globular shape having an average radius of 13 nm circa, with nanopores between them. This type of nanoporous structure with high roughness in its external surface is expected for thin films prepared by the method used here, in which the silica film is produced by using a sol-wet gel process followed by volatilization of the organic compounds [26–29]. The root-mean square roughness determined from AFM measurements over the 2 × 2 μm^2 selected areas corresponding to Fig. 2(a)–(c) are 0.54, 38.8 and 3.4 nm, respectively.

Fig. 3 shows the X-ray reflectivity curve of the analyzed sample. The critical angle - for which the value of the reflected intensity is equal to one half the intensity at incidence angle equal to zero - is α_{cfilm}=(0.19 ± 0.01)° [30]. The average density of the SiO_2 film determined from the known chemical composition and the value of the critical angle α_{cfilm} resulted ρ_{film}=(1.9 ± 0.1) g/cm^3. This density is lower than the density of non-porous amorphous SiO_2 materials (ρ_{SiO2}=2.20 g/cm^3), thus evidencing the porous nature of the thin film. Considering that nanopores in the thin film are embedded in a matrix of amorphous SiO_2, their volume fraction was determined by using the relation φ_{pore}=1-(ρ_{film}/ρ_{SiO2}) thus yielding φ_{pore}=0.14. This result confirms the nanoporous nature of the SiO_2 thin film deposited on Si wafer evidenced by our AFM analysis.

On the other hand, the curve plotted in Fig. 3 does not exhibit the characteristic oscillations at high angles that are expected for XRR curves associated to roughness-free thin films deposited on a flat substrate [30]. This confirms that the SiO_2 thin film and/or the Si wafer surface exhibit rather high surface roughness, as it also is evidenced in the AFM images shown in Fig. 2(b) and (c).

4.2. STEM

4.2.1. Evidences of nanoparticles and nanoplates buried in a Si(001) wafer
Fig. 4 shows a set of HAADF-STEM cross-sectional images of a Si (001) wafer substrate in which a 85 nm thick Ni-doped SiO_2 thin film was deposited, all these images being taken with the electron beam parallel to the Si[110] crystallographic direction.

In Fig. 4(a) we have indicated by a traced line (as a guide for the eye) the interface between the SiO_2 thin film and the rough Si(001) wafer. Two nanoplates are clearly apparent in Fig. 4(a), which are fully buried inside the Si wafer. One of them, on the left, is a side view of a hexagonal platelet with its large surface parallel to the Si(1–11) crystallographic plane and the other, on the right, has its large hexagonal surfaces parallel to the Si(111) crystallographic plane. We also notice that the nanoplates that are fully buried inside the Si wafer have their top side at about 85 nm far from the surface of the Si(001) wafer. This defines a 85 nm thick intermediate layer of Si(001) wafer characterized by an irregular morphology located between the bottom surface of the SiO_2
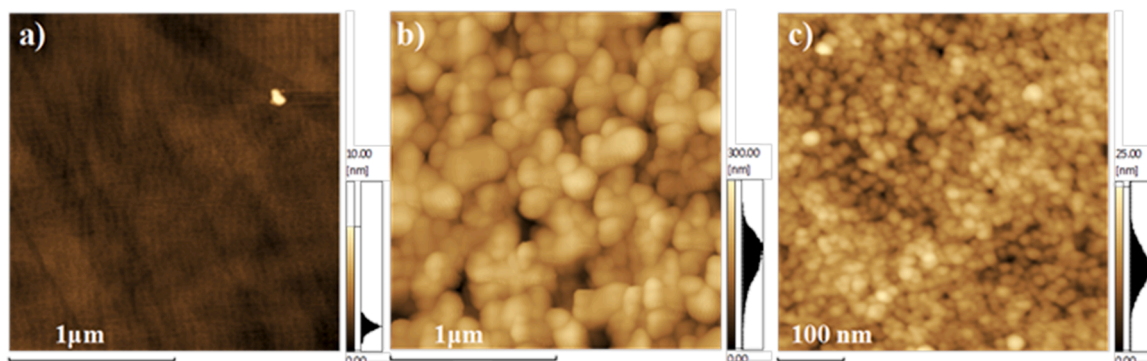

Fig. 1. Schematic view of the experimental setup used in GISAXS measurements.

Fig. 2. AFM topographic images of the surface of (a) the silicon wafer covered by its native oxide film after cleaning to remove organic contaminants (full z scale: 10 nm), (b) the same surface after being attacked with a concentrated solution of HF acid (full z scale: 300 nm), and (c) surface of the Ni-doped SiO$_2$ thin film deposited on Si wafer (full z scale: 25 nm). The image in (c) shows the SiO$_2$ film formed by a set of close-packed SiO$_2$ nanoparticles with spheroidal shape and average radius equal to 13 nm circa.
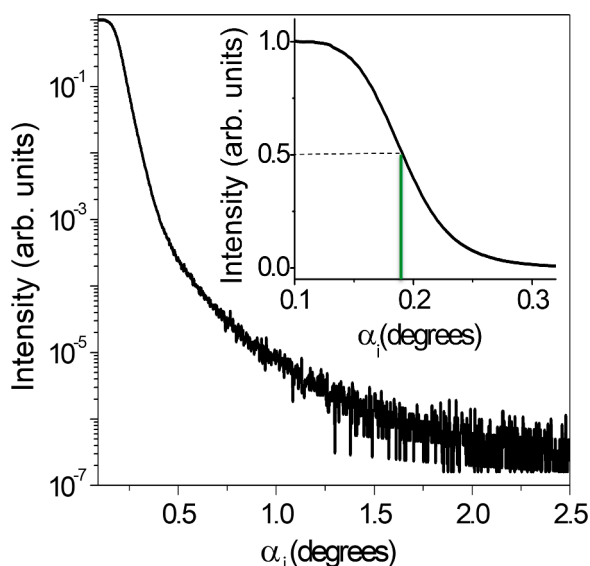

Fig. 3. XRR intensity produced by the Ni-doped SiO$_2$ thin film deposited on the Si(001) wafer. Inset: Detailed view of the XRR curve near the critical angle indicated by the vertical solid line at $\alpha_i = 0.19°$.

thin film and the layer containing the buried hexagonal nanoplates.

Fig. 4(b) is a magnified image of the cross sections of the SiO$_2$ thin film (on top), and the upper part of an intermediate Si(001) layer located close to the SiO$_2$:Si(001) interface (at the bottom). Inside the SiO$_2$ thin film we can notice the presence of a set of bright spots that we assigned to the presence of nearly spherical nanoparticles. In the intermediate layer we can notice the irregular shape of the interface between the SiO$_2$ thin film and the Si(001) wafer. The dark spots near the interface evidence the presence of porous volumes both in the deposited SiO$_2$ film and inside the silicon volume in the intermediate layer, close to the SiO$_2$:Si wafer interface.

Fig. 4(c) is a magnified image of a selected area of Fig 4(a) showing the nanostructure of the intermediate layer (on top) and the upper part of the cross section of a nanoplate (at the bottom). The image in Fig 4(b) shows that besides spherical nanoparticles located inside the SiO$_2$ thin film, another set of also nearly spherical nanoparticles with about the same size are embedded in the intermediate layer.

Fig. 4(d) is a XEDS image or chemical map corresponding to the same sample area as that shown in Fig. 4(c), which indicates the presence of nickel in both spherical nanoparticles and hexagonal nanoplates.

The nearly spherical nanoparticles located inside the thin film (Fig 4b) and those observed in the intermediate layer (Fig. 4c) are more precisely characterized in the next Section (4.2.2) by analyzing additional STEM images with a higher magnification. Moreover, the hexagonal nanoplates buried in the Si(001) wafer (Fig. 4a) are fully characterized in Section 4.2.3.

4.2.2. Crystallographic characterization of the spherical nanoparticles

Fig. 5(a) shows the cross section of the deposited SiO$_2$ thin film (on top), the intermediate layer of the Si wafer located close to the SiO$_2$:Si interface (central part) and a nearly frontal and partial view of a hexagonal nanoplate (at the bottom). A dashed line indicates the interface between the SiO$_2$ thin film and the Si(001) wafer. Darker irregular areas near the SiO$_2$:Si interface indicate the existence of a nanoporous (dendritic like) structure produced by corrosion effects due to the HF etching process.

Fig. 5(b) shows a magnified HR-STEM image of the area enclosed by a dashed square in Fig. 5(a). Two crystalline nanoparticles with different crystallographic orientations are clearly apparent inside the dashed circle and square.

Fig. 5(c) exhibits a magnified image of the largest crystalline nanoparticle located inside the dashed square shown in Fig. 5(b). We notice that this crystalline nanoparticle exhibits a nearly spherical shape and has a diameter of 6 nm circa.

Fig. 5(d) displays the Fast Fourier Transform (FFT) pattern of the image shown in Fig. 5(b). Most of the spots of the FFT pattern correspond to crystallographic planes of the Si[110] zone, while other spots indicated by white circles in Fig. 5(d) can be assigned to the crystalline nanoparticles embedded in the corroded layer in Si close to its external surface. As can be seen in Fig. 5(e), the crystallographic interplanar spacings associated to the spots are 1.76 Å and 2.03 Å, which correspond to the Ni(200) and Ni(111) crystallographic planes, respectively. This finding together with the result of chemical XEDS analysis (Fig. 4d) allowed us to safely conclude that the nearly spherical nanoparticles located inside the Si wafer and close to the SiO$_2$:Si interface are metallic Ni nanocrystals.

The high concentration of Ni nanocrystals near the SiO$_2$:Si interface is a consequence of the two-step deposition method in which a nickel nitrate layer is first deposited directly on the etched surface of Si wafer. After thermal treatment under reducing atmosphere (H$_2$) of the wafer covered by the thin film, reduced Ni species aggregate thus yielding a number of Ni nanoparticles both in the porous thin film and inside the porous volume of the Si wafer near the SiO$_2$:Si interface.

4.2.3. Crystallographic characterization of the hexagonal nanoplates

Fig. 6(a) shows a high-resolution STEM cross-sectional image of a Si: nanoplate interface, where the silicon phase (at the left) is darker than the nanoplate phase (at the right). The Si:nanoplate interface shown in Fig. 6(a) is parallel to the Si(-111) crystallographic plane.
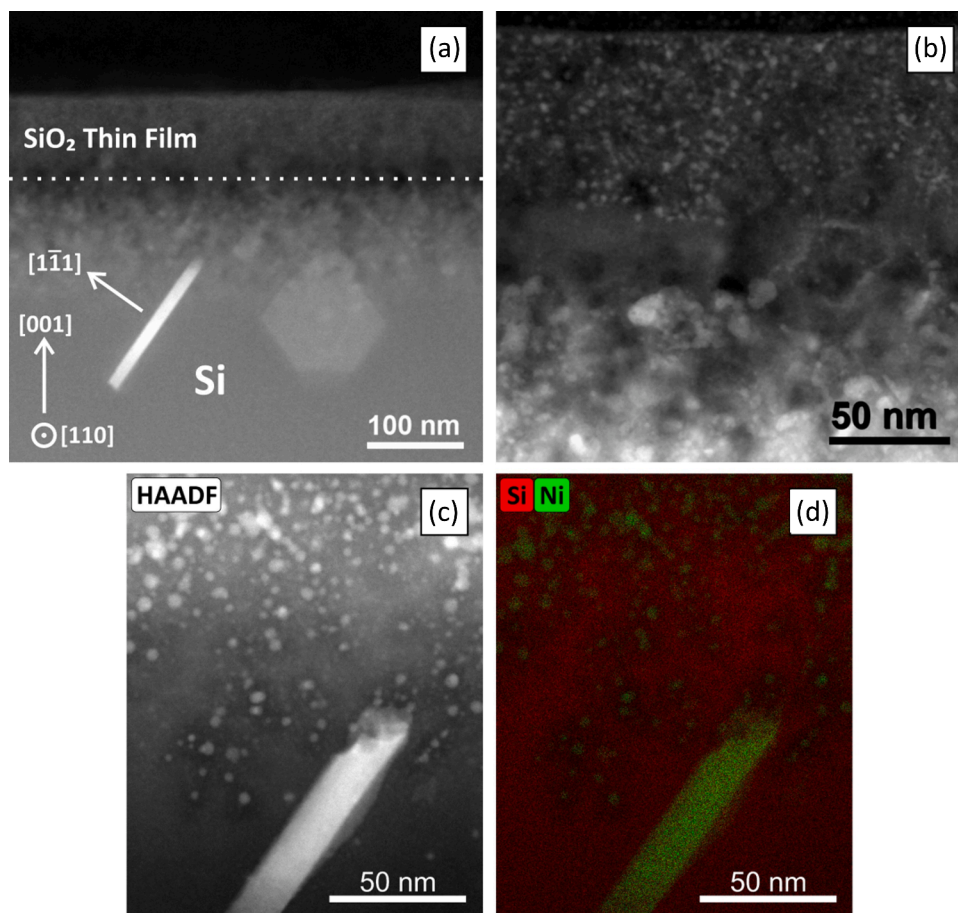
Fig. 4. (a) HAADF-STEM image of a cross-section of the Ni-doped SiO$_2$ thin film and Si wafer along the Si[110] crystallographic direction. The image shows on top (above the dashed line) the cross section of the SiO$_2$ thin film and, below, two nanoplates buried inside the Si wafer. The nanoplate on the left is a side-view with the large flat facet parallel to the Si (1–11) crystallographic plane. The hexagonal nanoplate on the right is an almost front-view parallel to the Si(111) plane. (b) Magnified image of the cross section of the SiO$_2$ thin film and the upper part of the Si(001) substrate showing on top the presence of small nanoparticles with nearly spherical shape inside the SiO$_2$ thin film. (c) Magnified image of a selected area of Fig. 4(a), showing on top the intermediate layer between the SiO$_2$ thin film and the layer where the hexagonal nanoplates are located. In Fig. 4b we can see the presence of nearly spherical nanoparticles inside the intermediate layer close to the external surface of the Si(001) wafer and also embedded in the SiO$_2$ thin film. (d) Chemical maps from XEDS-STEM of the same area as in 4(c) showing the spatial distribution of Ni (green) and Si (red). This image indicates that both the spherical particles and the nanoplates contain Ni atoms and evidences Si-depleted areas surrounding the spherical nanoparticles. (For interpretation of the references to color in this figure legend, the reader is referred to the web version of this article)
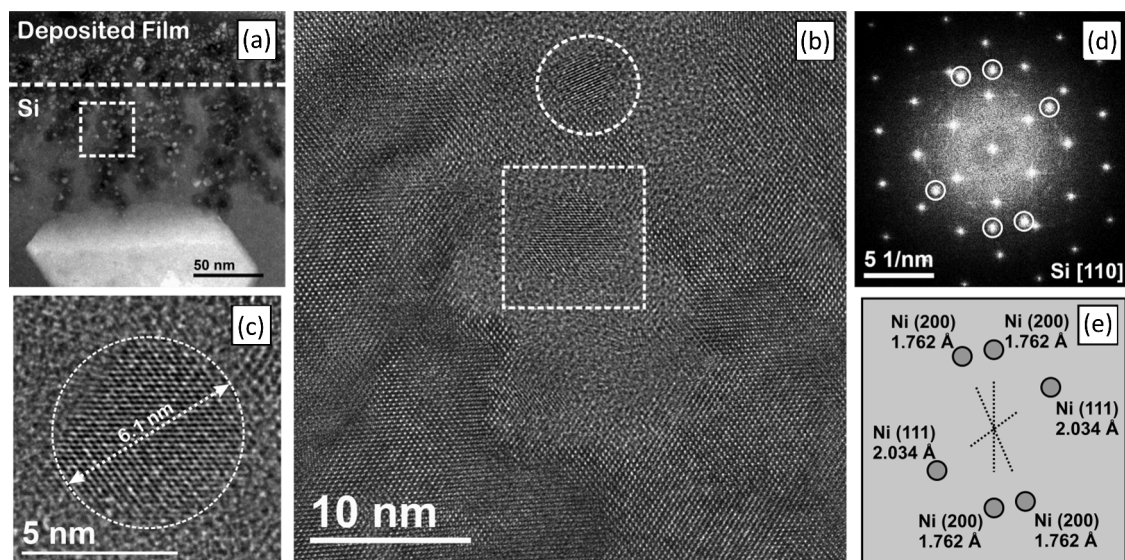

Fig. 5. (a) HAADF-STEM cross-sectional image of the deposited thin film and Si wafer close to the SiO$_2$:Si interface. The dashed line indicates the interface between the SiO$_2$ thin film and the Si rough surface. On top we can see the cross section of the SiO$_2$ thin film, the central part is the intermediate layer between the SiO$_2$ thin film and the layer in which the hexagonal nanoplates are located. At the bottom the upper part of an almost frontal view of a hexagonal nanoplate is apparent. (b) Magnified HR-STEM image of the area enclosed by a dashed square in Fig. 5(a). The dashed circle and square in Fig. 5(b) contain crystalline nanoparticles with different crystallographic orientations. (c) Magnified HR-STEM image of the dashed square containing the largest nanocrystal shown in Fig. 5(b). (d) Fast Fourier Transform of the image displayed in Fig. 5(b) showing the symmetric reflection spots associated to the Si[110] zone axis and some additional (encircled) reflections. (e) Indexing of the encircled spots shown in Fig 5(d) and the respective interplanar spacings which were assigned to Ni(200) and Ni(111) crystallographic planes.
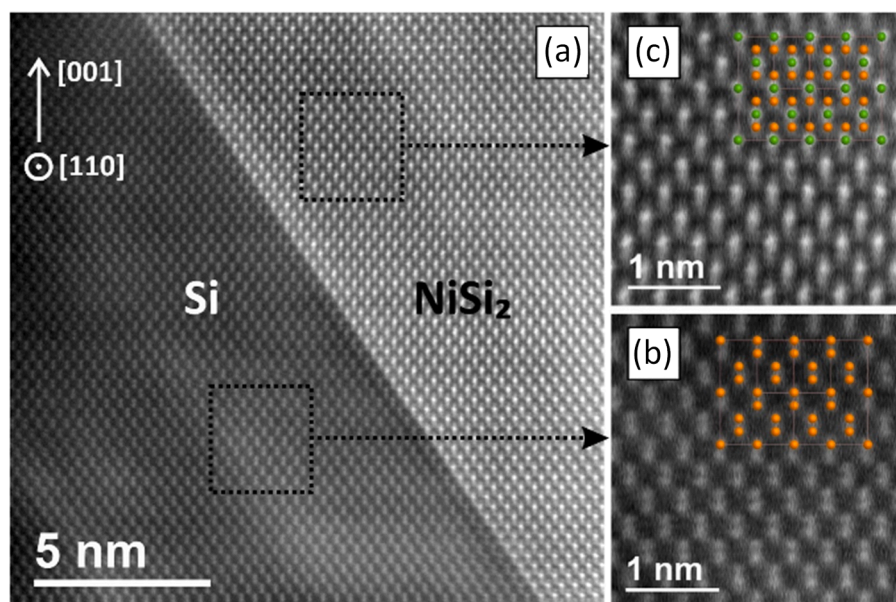
Fig. 6. HAADF-HR-STEM cross-sectional images of the interface between the Si wafer (left) and a $NiSi_2$ nanoplate (right). (a) Image taken with the electron beam along the Si[110] direction. The surface of contact between the Si and $NiSi_2$ structures is parallel to the Si(1–11) lattice plane. (b) Magnified image of the Si structure where the drawn orange solid circles indicate atom columns in the Si unit cell. (c) Magnified image of the $NiSi_2$ structure where the drawn green and orange circles indicate Ni and Si columns, respectively, in the $NiSi_2$ unit cell. (For interpretation of the references to color in this figure legend, the reader is referred to the web version of this article)

Fig. 6(b) exhibits a magnified view of the Si wafer projected along the Si[110] direction of the atomic structure. In this figure, the typical dumbbell-like structure of Si columns along the Si[110] with inter-atomic distance of 1.36 Å is clearly apparent.

A selected area of the hexagonal nanoplate showing atom columns along Si[110] is displayed in Fig. 6(c). The analysis of this image allowed us to conclude that the hexagonal nanoplates exhibit the cubic crystallographic structure of nickel disilicide ($NiSi_2$). The unit cell of the $NiSi_2$ structure depicted in Fig. 6(c) evidences a perfect match with the experimental image either for nickel columns (green circles) and for silicon columns (orange circles). A careful analysis of these HR-STEM images evidenced the presence of a 7A-type epitaxial interface between the lattices of the silicide nanoplates and that of the Si single crystalline host. This issue will be discussed in more detail in Section 5.

4.3. GISAXS analysis

4.3.1. General features

Once the nature, shape and approximate dimensions of the nanoparticles formed in the Si(001) wafer and in the deposited SiO_2 thin film - i.e, oriented hexagonal $NiSi_2$ thin nanoplates and nearly spherical Ni nanocrystals - were determined by HR-STEM, we conducted an additional study by the GISAXS technique. This scattering technique allowed us a more precise determination of the radius distribution of spherical Ni nanoparticles, and the dimensions and orientations of the hexagonal $NiSi_2$ nanoplates over a volume much larger than that probed by high resolution imaging techniques.

The GISAXS measurement was performed at room temperature using a sample consisting of a Si(001) wafer on which Ni-doped SiO_2 thin film was deposited after being held at 500 °C during 40 min. Notice that the sample studied by GISAXS was subjected to the same preparation procedure and same thermal annealing as the samples studied by STEM.

Fig. 7(a) shows a 2D GISAXS intensity pattern produced by a Si(001) wafer on which Ni-doped SiO_2 thin film was deposited after being held at 500 °C. The 2D GISAXS intensity pattern shows a strong isotropic scattering intensity mainly attributed to the presence of spherical Ni nanocrystals embedded in the thin film and in the intermediate layer of the Si(001) substrate close to the SiO_2:Si interface, as it is clearly apparent in the STEM images. These Ni nanocrystals are formed by uphill diffusion and aggregation - during the thermal treatment at 500 °C - of initially isolated Ni atoms in the Ni-doped SiO_2 thin film. Our analyses by AFM and XRR indicated that the SiO_2 thin film is nanoporous, thus an

additional contribution to the isotropic GISAXS intensity produced by the nanopores is also expected.

Superposed to the isotropic GISAXS intensity displayed in Fig. 7(a), an anisotropic petal-like contribution to the scattering intensity can be observed in the GISAXS pattern. This anisotropic contribution to the intensity is produced by oriented $NiSi_2$ nanoplates endotaxialy grown in Si single crystals, which were apparent in our HR-STEM images (Section 4.2). This type of anisotropic scattering was also previously observed in similar systems composed of a Si(001) wafer on which Co-doped thin films were deposited [21–23]. The growth of the $NiSi_2$ platelets occurs as a consequence of the thermal activated diffusion of Ni atoms that migrate from the thin film into silicon wafer.

The angles between the directions of the major axis of the two thin petals observed in the GISAXS pattern (Fig. 7a) and the normal to the Si (001) wafer surface are equal to 54.7°. Taking into account that the angle between the Si[001] direction and the four Si{111} crystallographic directions for cubic systems are also 54.7°, we concluded that the petals of anisotropic scattering are produced by the thin platelets parallel to planes of the Si{111} crystallographic form previously observed in the STEM images. More explicitly, this first analysis of the anisotropic part of the GISAXS patterns of the studied system - showing two thin petal-like images as shown in Fig. 7(a) - strongly suggests that the scattering intensity is produced by a set of thin nanoplates with their large flat surfaces parallel to one of the four lattice planes of the Si{111} crystallographic form in agreement with STEM results.

The weak asymmetry observed in the anisotropic contribution to scattering intensity pattern displayed in Fig. 7(a), with respect to a vertical line at $q_\parallel = 0$, is in fact an *a priori* expected effect because both (i) the incidence angle between the direction of the incoming X-ray beam and the wafer surface - i. e. with respect to the crystallographic Si (001) planes – and (ii) ϕ angle, even being small, are different from zero. Obviously, this effect does not affect the scattering intensity patterns produced by randomly oriented nanopores of any shape, or by the spherical Ni nanoparticles.

4.3.2. Modelling of GISAXS intensity

The GISAXS profiles in the q_y - q_z plane were modeled considering that the total intensity is composed of three independent contributions from (i) a set of spatially uncorrelated spherical Ni nanocrystals exhibiting some radius dispersion embedded in the deposited Ni-doped SiO_2 thin film and in the intermediate layer of the Si(001) substrate, (ii) a dilute set of hexagonal $NiSi_2$ thin nanoplates with their large surfaces
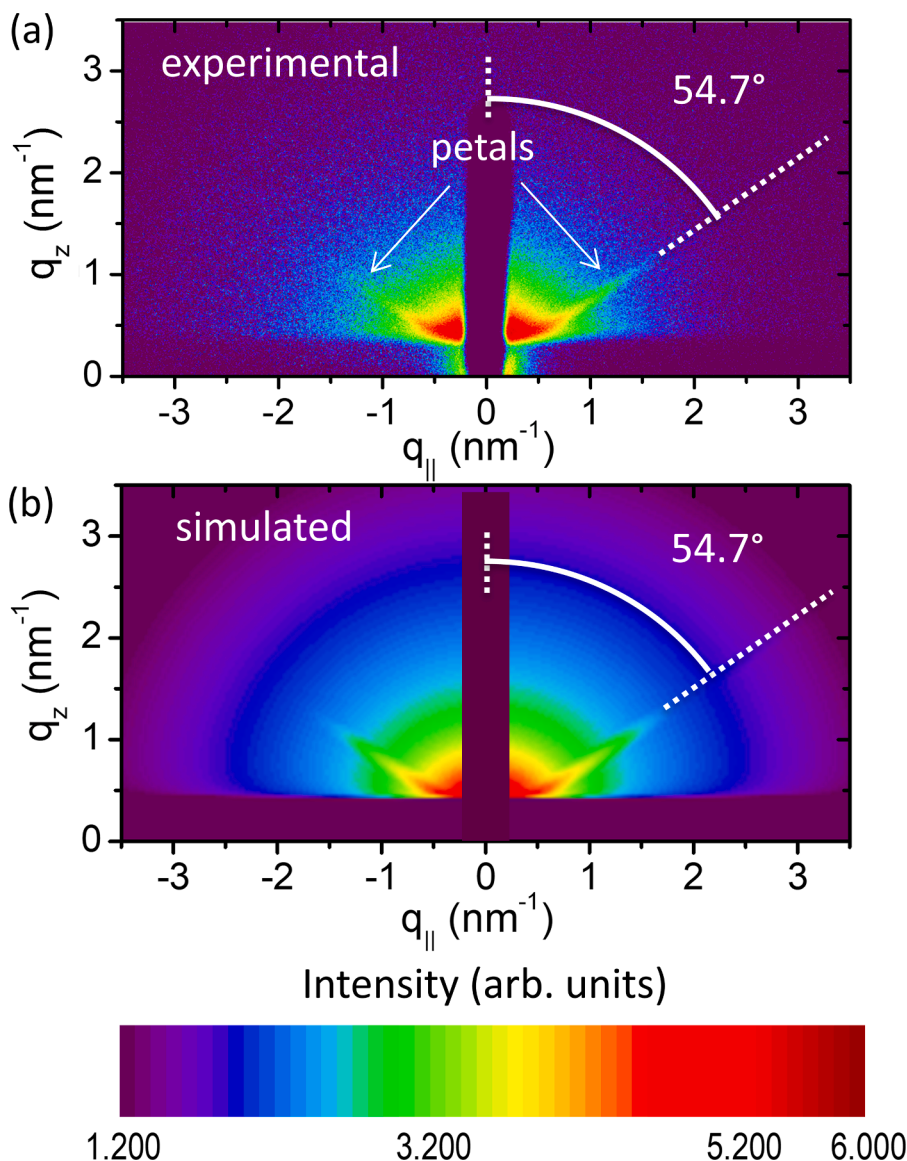
Fig. 7. (a) GISAXS intensity patterns due to a Si(001) wafer in which a Ni-doped SiO_2 thin film was deposited. An anisotropic contribution to the total GISAXS intensity – showing petals-like shaped features forming a 54.7° angle with q_z axis - indicate the presence of well oriented nanoplates having their large surfaces parallel to one of planes of the Si{111} crystallographic form. (b) Simulated 2D GISAXS intensity determined from the best fit of Eq. (2) to the experimental intensity. (For interpretation of the references to color in this figure legend, the reader is referred to the web version of this article)

parallel to one of the four lattice planes of the Si{111} crystallographic form and (iii) a set of small nanopores embedded in the deposited SiO_2 thin film produced by sol-gel method. Spherical Ni nanocrystals and thin hexagonal $NiSi_2$ nanoplates are clearly apparent in the HR-STEM images, their crystallographic characterizations being described in Sections 4.2.2 and 4.2.3, respectively, while the very small nanopores embedded in the deposited SiO_2 thin films were not detected in HR-STEM images but - as it will be reported in Section 4.3.3 - the presence of small nanopores is a typical and expected feature in thin films prepared by the sol-gel procedure.

Our HR-STEM analysis indicated the presence of spherical Ni nanocrystals embedded in the SiO_2 thin film and also inside an intermediate layer between the SiO_2 thin film:Si wafer interface and the layer containing the buried hexagonal $NiSi_2$ nanoplates. As an approximation for modeling of the GISAXS intensity we assumed that the nanopores also have a spherical shape. In order to account for the dispersion in size of the Ni nanocrystals and nanopores the isotropic part of the GISAXS intensity was modeled by assuming that the radius distribution function of Ni nanoparticles and nanopores can be well described by lognormal functions (see SM-Section C).

The analyses of several STEM images containing thin $NiSi_2$ platelets indicated some dispersion in their thickness t. For this reason, for modeling the GISAXS intensity, we have assumed a Gaussian radius distribution to describe the dispersion in nanoplate thicknesses. On the other hand, STEM images also indicated some dispersion in the lateral side L of the hexagonal $NiSi_2$ nanoplates. Nevertheless, we have also noticed that the width of intensity profiles along the direction parallel to the surface of nanoplates – which is related to the L values - is very small. Therefore, a more precise analysis accounting for a detailed description of the dispersion in L values was not performed.

Taking into consideration all the assumptions described above, the total GISAXS intensity is given by:

$$I(q) \propto |T(\alpha_i)|^2 \, |T(\alpha_f)|^2 \left\{ \left[c \frac{(\rho_{Ni} - \rho_{SiO_2})^2}{A_1(q_z)} + (1-c) \frac{(\rho_{Ni} - \rho_{Si})^2}{A_2(q_z)} \right] \times \right.$$

$$\int_{R=0}^{\infty} \left(\frac{4}{3}\pi R^3\right)^2 \left|F_{sph}(q_\parallel, \widetilde{q}_z, R)\right|^2 N_{Ni}(R) dR +$$

$$\frac{(\rho_{SiO_2})^2}{A_1(q_z)} \int_{R=0}^{\infty} \left(\frac{4}{3}\pi R^3\right)^2 \left|F_{sph}(q_\parallel, \widetilde{q}_z, R)\right|^2 N_{pores}(R) dR +$$

$$\left. \frac{1}{4} \frac{(\rho_H - \rho_{Si})^2}{A_3(q_z)} \int_{t=0}^{\infty} \sum_{i=1}^{4} \left|H_i(\alpha, \phi, q_\parallel, \widetilde{q}_z, L, t)\right|^2 N_H(t) dt \right\} \qquad (2)$$

where $|T(\alpha_i)|^2$ and $|T(\alpha_f)|^2$ are the transmission functions accounting for the intensity of the refracted and scattered beams inside the SiO$_2$ film; α_i and α_f are the grazing-incidence angles of the primary and scattered beams, respectively, c is the fraction of Ni nanoparticles in SiO$_2$ thin film, H_i is the scattering amplitude due a hexagonal silicide nanoplate with lateral size L and thickness t, and $N_H(t)dt$ is the number of nanoplates with thickness between t and $t + dt$. The indexes i (from 1 to 4) refer to the four possible orientations of the platelets - which are assumed to be all of them equally probable - corresponding to the nanohexagons parallel to one of the four possible orientations of the planes of the Si{111} crystallographic form; $F_{sph}(R)$ is the scattering amplitude associated to Ni nanoparticles and nanopores with radius R and radius distribution functions $N_{Ni}(R)$ and $N_{pores}(R)$, respectively. A_1 and A_2 are the functions that account for the attenuation of the GISAXS intensity produced by scattering objects embedded in SiO$_2$ thin films and intermediate layer, respectively, and A_3 is the attenuation function of the GISAXS intensity due to NiSi$_2$ platelets buried in the Si wafer. The procedure used to calculate these functions is described in Sec. A of Supplementary Material (SM). The electron densities ρ_{Ni}, ρ_{SiO_2}, ρ_H and ρ_{Si} corresponds to Ni, SiO$_2$, NiSi$_2$ and Si, respectively, α is the angle between the direction normal to sample surface and the crystallographic Si[001] direction, $\widetilde{q}_z$ is the component of scattering vector normal to sample surface and $q_\parallel = \sqrt{q_x^2 + q_y^2}$. The functions that describe the scattering amplitude of a regular hexagon H_i with its large surfaces parallel to Si{111} crystallographic planes is given in Eqs. S9 and S10 of Supplementary Material. These equations assume that the projection of the incident beam on the plane perpendicular to the Si[001] direction coincides with the Si[011] crystallographic direction. The scattering amplitude produced by a homogeneous sphere (particle or pore) of radius R, F_{sph}, is given in the Eq. S6 and S7 of the Supplementary Material.

Fig. 7(a) displays the experimental 2D GISAXS pattern produced by the studied sample and Fig. 7(b) shows the simulated 2D GISAXS intensity pattern calculated from the best fitting of Eq. (2) to the several 1D GISAXS curves for different q_z values plotted in Fig. 8. The different curves in Fig. 8 show somewhat weak peaks - related to the contribution from the NiSi$_2$ nanoplates - superposed to a broader and strong isotropic scattering intensity produced by the Ni nanocrystals and nanopores. The peaks at left and right sides in Fig. 8 associated to the NiSi$_2$ nanoplates are expected to be symmetric with respect to $q_\parallel = 0$, the observed asymmetry being due to an offset of the azimuthal angle of orientation of the studied sample with respect to the Si[110] direction. This offset angle was included in the modeling GISAXS function and determined by applying the best fitting procedure.

The good agreements between the experimental scattering intensity and the simulated GISAXS intensity observed in Fig. 7 and more precisely in Fig. 8 confirm the validity of the structural model derived from our STEM analysis that was used to describe the shape and orientations of NiSi$_2$ nanoplates grown in the Si(001) wafer.
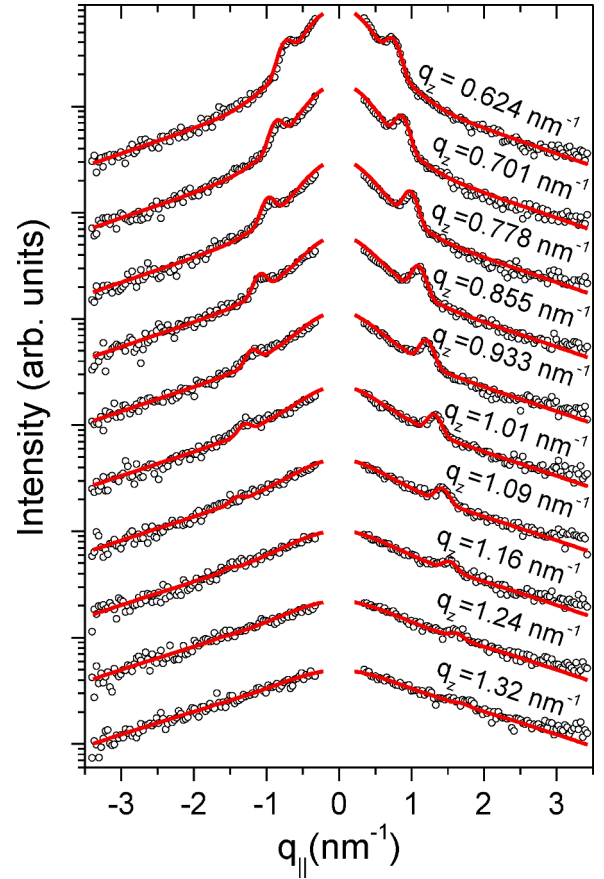

Fig. 8. Experimental GISAXS intensity profiles $I \times q_\parallel$ extracted from the 2D pattern displayed in Fig. 7 for the selected values of q_z produced by a Si(001) wafer in which a Ni-doped SiO$_2$ thin film was deposited (symbols). Calculated GISAXS intensity curves corresponding to the best fit of Eq. (2) to the experimental data (solid lines).

4.3.3. Radius distribution of spherical Ni nanocrystals and nanopores

According to the conclusions from our HR-STEM analyses (Section 4.2.1), we have assumed that the main contribution to the isotropic part of the GISAXS intensity is produced by spherical Ni nanocrystals located inside the thin film and intermediate layer close to the SiO$_2$:Si interface. On the other hand, the analysis of the HR-STEM images suggested that the Ni nanocrystals exhibit some radius dispersion.

An additional contribution to the isotropic component of the GISAXS intensity was expected to be produced by very small nanopores embedded in the deposited SiO$_2$ thin film. Notice that the presence of nanopores is a typical feature in SiO$_2$ films prepared by the sol-gel method [31]. The sizes of nanopores embedded in a SiO$_2$ thin film produced by the sol-gel method depend - among other parameters - on the temperature and time of thermal treatment. We assumed that the nanopores embedded in the thin film also exhibit a spherical shape.

Taking in consideration the arguments mentioned above, we concluded that the isotropic part of the GISAXS intensity could be well described by two lognormal radius distribution functions corresponding to larger Ni nanocrystals and smaller nanopores.

Fig. S1 of Supplementary Material displays the experimental GISAXS intensity profile in linear scale for $q_z = 0.855$ nm^{-1}. We can notice in Fig. S1 the presence of two narrow and rather weak peaks produced by the anisotropic set of NiSi$_2$ nanoplates. We can also notice a strong contribution to isotropic GISAXS intensity that we assigned to Ni nanocrystals and a relatively weak contribution due to the nanopores embedded in the SiO$_2$ thin film.

A preliminary analysis of the broad and weak GISAXS intensity profile associated with the presence of very small pores indicated that

their average radius is 0.5–0.7 nm circa. However, we have noticed that the relevant part the of GISAXS produced by these small nanopores is expected to extend up to a q value much higher than the highest q used in our GISAXS measurements, for which the maximum q is equal to 3.5 nm^{-1}. Since the goal of this work was the structural and morphologic characterization of Ni nanocrystals and NiSi$_2$ nanoplates, a detailed and more precise analysis of the size distribution of nanopores embedded in the SiO$_2$ film was not performed.

The volume weighted radius distribution functions $V_{Ni}(R) = (4\pi/3) R^3 N_{Ni}(R)$ of the nearly spherical Ni nanocrystals embedded in the SiO$_2$ film and in the intermediate layer close to the SiO$_2$:Si interface was determined by the best fitting of the isotropic part of Eq. (2) to the isotropic contribution of the experimental GISAXS intensity displayed in Fig. 8, each of them corresponding to a particular q_z value. The good results of our fitting procedure shown in Fig. 8 indicated that our assumptions of the presence of a population of Ni nanocrystals and another population of small nanopores and a lognormal radius distribution for Ni nanocrystals are reasonable.

The volume weighted radius distribution function derived from our fitting calculation and related to the spherical Ni particles, $V_{Ni}(R)$, is shown in Fig. 9. The relevant parameters derived from the best fitting procedure, namely the average radius and the standard deviation, associated to the lognormal radius distribution, are reported in Table 1.

As reported in Table 1, the average radius and standard deviation associated to the lognormal function referring to Ni nanocrystals and determined from our GISAXS analysis are 1.7 nm and 0.9 nm, respectively. On the other hand, the average radius and standard deviation derived from HR-STEM images are 1.56 nm and 0.7 nm, respectively, in good agreement with the results derived from GISAXS measurements.

4.3.4. Thickness and maximum diameter of the hexagonal NiSi$_2$ nanoplates

The GISAXS patterns plotted in Fig. 8 evidence that the major component of the experimental GISAXS intensity is isotropic and is produced by spherical Ni nanocrystals and nanopores while only a minor anisotropic component is produced by the oriented NiSi$_2$ nanoplates. In order to improve the accuracy of our quantitative analysis of the part of GISAXS intensity pattern associated to the hexagonal NiSi$_2$ nanoplates, we have subtracted the isotropic contribution from the total experimental intensity, and the difference functions were plotted in Fig. 10 (circles). The experimental GISAXS profiles separately plotted in Fig. 10 are exclusively related to the hexagonal NiSi$_2$ nanoplates. Thus, the relevant size parameters were determined by best fitting only the third term of Eq. (2) to the GISAXS profiles displayed in Fig. 10.

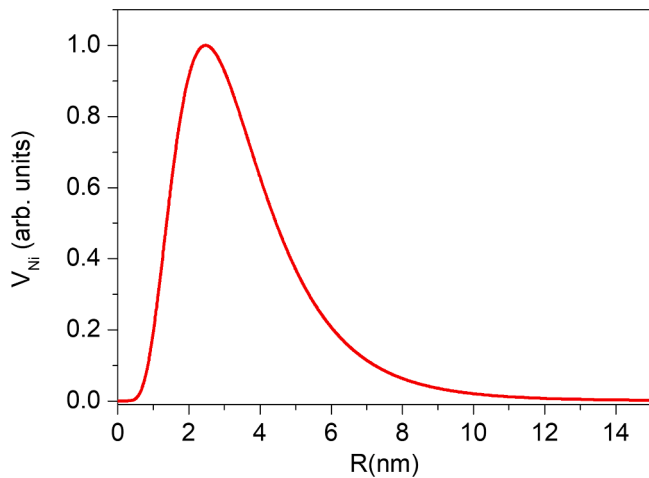The solid lines in Fig. 10 correspond to the best fitting of the last term

Table 1

Size parameters of spherical Ni nanocrystals determined from HR-STEM images and GISAXS measurements; $\langle R \rangle_{Ni}$ is the average radius and σ_{RNi} the standard deviations associated to the radius distribution plotted in Fig. 9.

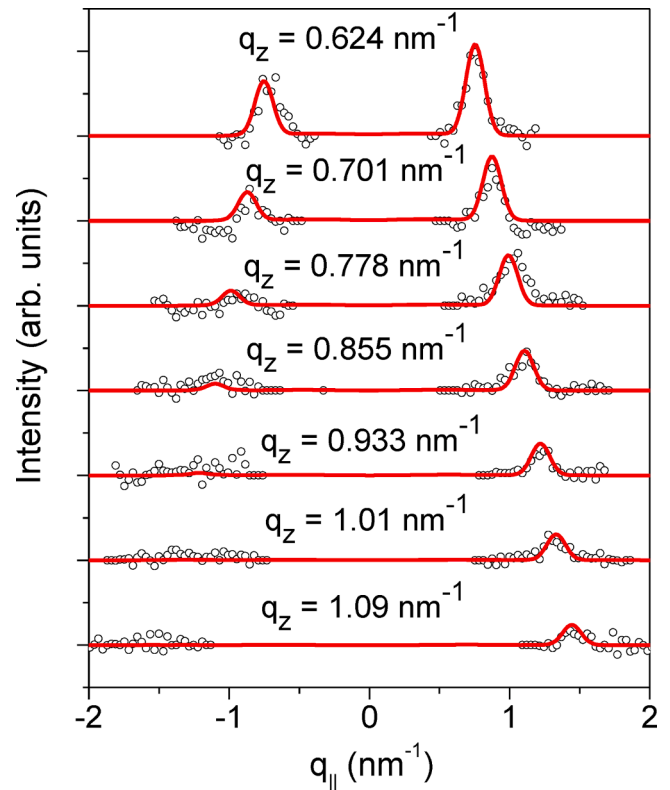| Nano-objects	Size parameters	HR-STEM	GISAXS
Spherical Ni nanocrystals	$\langle R \rangle_{Ni}$ (nm)	1.56 ± 0.05	1.7 ± 0.2
	σ_{RNi} (nm)	0.7 ± 0.1	0.9 ± 0.3

Fig. 10. Experimental GISAXS intensity profiles $I \times q_{\parallel}$ after subtraction of the isotropic scattering intensity for selected q_z values (symbols). These intensity profiles correspond to the anisotropic contribution to the total scattering intensity exclusively produced by the NiSi$_2$ hexagonal nanoplates formed inside the Si wafer. Calculated GISAXS intensity curves corresponding to the best fit of the last term of Eq. (2) to the experimental intensity profiles (solid lines).

Table 2

Main structural features and parameters of NiSi$_2$ nanoplates determined from HR-STEM images and GISAXS measurements; $\langle t \rangle$ and $\langle D \rangle = 2\langle L \rangle$ are average values and σ_t and σ_D are standard deviations associated to the distributions of thickness and maximum diameter values, respectively.

Nano-objects	Size parameters	HR-STEM	GISAXS
	Average thickness $\langle t \rangle$ (nm)	12.9 ± 0.6	12 ± 3
	Standard deviation of thicknesses σ_t (nm)	1.8 ± 0.3	3.5 ± 0.9
	Average maximum diameter $\langle D \rangle$ (nm)	146 ± 8	118 ± 4
	Standard deviation of maximum diameters σ_D (nm)	40 ± 12	—

in Eq. (2) - related to the NiSi$_2$ nanoplates - to the experimental difference intensity functions. The main features related to the NiSi$_2$ nanoplates derived from the analyses of imaging techniques and from GISAXS measurement are reported in Table 2. The average thickness and its standard deviation of NiSi$_2$ nanoplates derived from our GISAXS results are 12.0 nm and 3.5 nm, respectively, in good agreement with the values

Fig. 9. Volume weighted lognormal radius distributions derived from our GISAXS results corresponding to Ni nanoparticles embedded in the SiO$_2$ thin film and inside the Si wafer close to its external surface.

derived from our analyses of HR-STEM images, namely 12.9 nm and 1.8 nm, respectively, which were derived from the direct measurements of the dimensions of eleven different $NiSi_2$ nanoplates. The average maximum diameter of the hexagonal $NiSi_2$ nanoplates $\langle D \rangle$ - where $\langle D \rangle = 2\langle L \rangle$, $\langle L \rangle$ being the average value of L - derived from our GISAXS results is 118 nm while the average diameter and standard deviation derived from the analyses of several nanoplates observed in STEM images are 146 nm and 40 nm, respectively, which indicate a reasonable agreement between the results derived from HR-STEM and GISAXS techniques.

5. Discussion and conclusions

The evidences from our experimental HR-STEM and GISAXS results demonstrate that the use of the novel preparation procedure proposed in this work leads to the formation of (i) a 2D array consisting of a number of thin hexagonal $NiSi_2$ nanoplates buried inside a Si(001) wafer and (ii) a set of nearly spherical Ni nanocrystals embedded in the deposited SiO_2 thin film and also inside a narrow intermediate layer near the external surface of the single crystalline Si wafer. Both, our quantitative analyses of HR-STEM images and the anisotropic contributions to GISAXS patterns, demonstrate that the $NiSi_2$ nanoplates buried in the Si(001) wafer exhibit a nearly hexagonal shape with their larger surfaces parallel to one of the four lattice planes of the Si{111} crystallographic form and are coherently related to the lattice of the single crystalline Si wafer.

The growth processes of $NiSi_2$ platelets and Ni nanocrystals in Si wafers are thermally activated and involve the successive diffusion of initially dispersed Ni atoms through the volume of the deposited SiO_2 thin film, across the SiO_2:Si interface and through a thin volume close to the external surface of the Si wafer.

The average thickness of the $NiSi_2$ platelets determined from GISAXS analysis reported in Table 2 agrees well with the value of the same parameter determined from HR-STEM analysis. On the other hand, the maximum diameter of the silicide nanoplates derived from GISAXS analysis is somewhat smaller than the same parameter determined from HR-STEM. This minor discrepancy can be attributed to the great difference in the number of $NiSi_2$ nanocrystals probed by these two techniques.

GISAXS patterns referring to $NiSi_2$ nanoplates are similar as those reported by previous GISAXS studies of $CoSi_2$ nanoplates embedded in Si wafers [21–23]. However, some differences regarding the nanostructures of $NiSi_2$:Si and $CoSi_2$:Si can be noticed. As a matter of fact, our HR-STEM images of a $NiSi_2$:Si array evidence that the $NiSi_2$ hexagonal nanoplates are totally buried inside - and not in contact with the surface of - the Si wafer while the nanoplates in the $CoSi_2$:Si array system are close to the external surface, with one of their hexagonal sides in contact with the SiO_2:Si interface.

The formation of coherent $NiSi_2$ nanoplates is favored in single crystalline Si host because their cubic lattice parameters are similar to that of cubic Si crystals. Endotaxial growth of $NiSi_2$ in silicon has previously been reported but in these cases the authors have used different preparation procedure and obtained $NiSi_2$ nanowires instead of nanoplates [14,15,20].

The coherent interfaces between the crystallographic lattices of the single crystalline Si wafer and that of transition-metal silicides (Si: $TMSi_2$) were extensively studied by several authors [20,32,33], who reported different types of interface structures. Here, from a careful analysis of the HR-STEM image, we have concluded that the interface $NiSi_2$(111):Si(111) is of 7A-type. This implies that Ni atoms located at the interface are in 7-fold coordination with Si atoms, and the silicide structure is in-line with the Si [111] axis. This result is different from that previously determined for the interface between single crystalline Si and $CoSi_2$ nanoplates, which exhibit an 8B-type interface structure [21].

The formation of 7A and 7B-type interfaces is expected in the case of $NiSi_2$(111):Si(111) because among the several possible types of interfaces these are those having the smallest values for energy density [32]. Moreover, the difference in formation energy of these interfaces

(7A and 7B) is small (0.01 eV per Ni-pair), this being the more probable reason for the fact that both types (7A and 7B) were previously observed for $NiSi_2$(111):Si(111) interfaces, in some cases in the same system [33]. Conclusions from this study [33] also suggest that for the endotaxial growth of Ni disilicide on Si(001) a $NiSi_2$:Si 7A-type interface is preferentially nucleated in absence of residual oxides while residual oxides on Si leads to 7B-type interface. On the other hand, in the case of $CoSi_2$(111):Si(111) the interface configuration with the lowest energy is the 8B-type [32] in accordance with our previous observation [21]. This finding confirms that interfaces with smaller energy density are the most probable for $NiSi_2$(111):Si(111) and $CoSi_2$(111):Si(111) interfaces for the preparation methods described here.

Our STEM images and GISAXS results also demonstrate the existence of nearly spherical Ni nanocrystals embedded in the SiO_2 thin film and inside an intermediate layer between the external surface of the Si wafer and the layer in which the $NiSi_2$ nanoplates are located.

Our analyses of STEM images also show strong corrosion effects on the surface of the Si wafer produced by the process of HF etching used to remove the native Si oxide. The etching process promotes the formation of an irregular and rough layer close to the interface between the SiO_2 thin film and the Si wafer, which contains nearly spherical Ni nanocrystals. Notice that in the case of the previously studied $CoSi_2$-based arrays [21–23] - not submitted to HF etching - no Co nanocrystals embedded inside the Si(001) wafer were detected.

The remarkable features related to the observed differences between the different procedures for preparation of $CoSi_2$ and $NiSi_2$ nanoplates in a Si(001) wafer are associated to the effects produced by the native SiO_2 oxide layer, which covers the Si wafer on the atomic diffusion process. In the process previously applied for growing $CoSi_2$ nanoplates, the Co-doped SiO_2 thin film was deposited on a Si(001) wafer without previously removing the native oxide layer, while in the present case the growth of $NiSi_2$ nanoplates was successfully achieved only after removal of the oxide native layer by HF etching. This indicates that the diffusion coefficient of Ni atoms through the SiO_2 layer is much lower than that of Co atoms. The deposition of the Ni-doped thin film directly on Si (after native Si oxide removal) used in the preparation method described here may also be connected to the fact that the minimum temperature ($T_{min} \sim 350$ °C) needed for a significant growth of $NiSi_2$ nanoplates is much lower than the temperature needed for the formation of $CoSi_2$ nanoplates ($T_{min} \sim 700$ °C) for which the Co-doped thin film was directly deposited on the Si wafer without previous removal of the native Si oxide.

Experimental results reported in previous works in which $NiSi_2$ nanoinclusions were formed inside individual grains in a polycrystalline Si film showed that these nanocomposites are promising candidates to be used as a thermoelectric material [9,34–36]. On the other hand, the Si:Si interfaces between silicon grains in polycrystalline films are expected to increase the scattering of conduction electrons thus leading to a worsening of the thermoelectric properties. The absence of incoherent Si:Si interfaces in the nanocomposites consisting of $NiSi_2$ nanoplates coherently grown in single crystalline Si wafers studied in the present work may lead to the development of new nanostructures, with electrical transport properties better than those of nanocomposites in which nanoinclusions of $NiSi_2$ are embedded in polycrystalline Si films. In addition, the described novel preparation procedure does not require expensive deposition methods and in view of environmental issues the substitution of Co by Ni is desirable.

The relevant effects of different chemical parameters and thermal conditions on the final nanostructures of the studied materials were not quantitatively determined. In order to achieve a reliable control of the final nanostructures and verify the reproducibility of different experiments, additional systematic investigations under different preparation conditions are required.

Declaration of Competing Interest

The authors declare that they have no known competing financial interests or personal relationships that could have appeared to influence the work reported in this paper.

Acknowledgment

Supplementary materials

Supplementary material associated with this article can be found, in the online version, at doi:10.1016/j.surfin.2022.101763.

References

[1] G. She, H. Liu, L. Mu, W. Shi, H. Li, J. Wu, Z.M. Wang, Synthesis, properties, and applications of one-dimensional transition metal silicide nanostructures. Silicon-Based Nanomater, Springer, New York, NY, 2013, pp. 265–325, https://doi.org/10.1007/978-1-4614-8169-0_12.

[2] M. Yengui, D. Riedel, Evidence of low Schottky barrier effects and the role of gap states in the electronic transport through individual CoSi$_2$ silicide nanoislands at low temperature (9K), J. Phys. Chem. C 119 (2015) 22700–22708, https://doi.org/10.1021/acs.jpcc.5b06816.

[3] O. Nakatsuka, A. Suzuki, A. Sakai, M. Ogawa, S. Zaima, Electrical properties of epitaxial NiSi$_2$/Si contacts with extremely flat interface formed in Ni/Ti/Si(001) system, Microelectron. Eng. 83 (2006) 2272–2276, https://doi.org/10.1016/j.mee.2006.10.009.

[4] Y. Tamura, R. Yoshihara, K. Kakushima, H. Nohira, O. Nakatsuka, P. Ahmet, Y. Kataoka, A. Nishiyama, N. Sugii, K. Tsutsui, K. Natori, T. Hattori, H. Iwai, Physical and electrical properties of ultra-thin nickel silicide Schottky diodes on Si (100), J. Phys. Conf. Ser. 417 (2013), 012015, https://doi.org/10.1088/1742-6596/417/1/012015.

[5] F.F. Zhao, J.Z. Zheng, Z.X. Shen, T. Osipowicz, W.Z. Gao, L.H. Chan, Thermal stability study of NiSi and NiSi$_2$ thin films, Microelectron. Eng. 71 (2004) 104–111, https://doi.org/10.1016/j.mee.2003.08.010.

[6] T. Meyer, M. Klemenc, T. Graf, H. von Känel, Self-organization in Si/CoSi$_2$(111) heteroepitaxy, J. Vac. Sci. Technol. B Microelectron. Nanometer Struct. 17 (1999) 1848, https://doi.org/10.1116/1.590837.

[7] Q.T. Zhao, P. Kluth, H.L. Bay, St. Lenk, S. Mantl, Nanopatterning of epitaxial CoSi$_2$ using oxidation in a local stress field and fabrication of nanometer metal-oxide-semiconductor field-effect transistors, J. Appl. Phys. 96 (2004) 5775–5780, https://doi.org/10.1063/1.1808246.

[8] Y.L. Jiang, X.P. Qu, G.P. Ru, B.Z. Li, Schottky barrier height lowering induced by CoSi$_2$ nanostructure, Appl. Phys. A 99 (2010) 93–98, https://doi.org/10.1007/s00339-009-5516-4.

[9] N. Uchida, Y. Ohishi, Y. Miyazaki, K. Kurosaki, S. Yamanaka, T. Tada, Thermoelectric properties of (100) oriented silicon and nickel silicide nanocomposite films grown on Si on insulator and Si on quartz glass substrates, Mater. Trans. 57 (2016) 1076–1081, https://doi.org/10.2320/matertrans.E-M2016807.

[10] L.V. Bondarenko, A.Y. Tupchaya, A.N. Mihalyuk, S.V. Eremeev, A.V. Matetskiy, N.V. Denisov, Y.E. Vekovshinin, A.V. Slyshkin, D.V. Gruznev, A.V. Zotov, A.A. Saranin, Fabrication and characterization of a single monolayer NiSi$_2$ sandwiched between a Tl capping layer and a Si(111) substrate, 2D Mater. 7 (2020), 025009, https://doi.org/10.1088/2053-1583/ab6495.

[11] Y. Zhou, M. Su, A. Dou, Y. Liu, Facile synthesis of Si/NiSi$_2$/C composite derived from metal-organic frameworks for high-performance lithium-ion battery anode, J. Electroanal. Chem. 873 (2020), 114398, https://doi.org/10.1016/j.jelechem.2020.114398.

[12] Y.H. Huang, H.C. Lin, S.L. Cheng, Fabrication of vertically well-aligned NiSi$_2$ nanoneedle arrays with enhanced field emission properties, J. Phys. Chem. Solids 150 (2021), 109892, https://doi.org/10.1016/j.jpcs.2020.109892.

[13] S.Y. Chen, L.J. Chen, Nitride-mediated epitaxy of self-assembled NiSi$_2$ nanowires on (001)Si, Appl. Phys. Lett. 87 (2005), 253111, https://doi.org/10.1063/1.2149970.

[14] J.F. Lin, J.P. Bird, Z. He, P.A. Bennett, D.J. Smith, Signatures of quantum transport in self-assembled epitaxial nickel silicide nanowires, Appl. Phys. Lett. 85 (2004) 281–283, https://doi.org/10.1063/1.1769583.

[15] P. Zu-Lin, S. Liang, D. Luo-Gen, Transition metal silicide nanowires growth and electrical characterization, Chin. Phys. Lett. 26 (2009), 127301, https://doi.org/10.1088/0256-307X/26/12/127301.

[16] X. Chen, J. Guan, G. Sha, Z. Gao, C.T. Williams, C. Liang, Preparation and magnetic properties of single phase Ni$_2$Si by reverse Rochow reaction, RSC Adv. 4 (2014) 653–659, https://doi.org/10.1039/C3RA43460E.

[17] T.T. Tran, C. Lavoie, Z. Zhang, D. Primetzhofer, *In-situ* nanoscale characterization of composition and structure during formation of ultrathin nickel silicide, Appl. Surf. Sci. 536 (2021), 147781, https://doi.org/10.1016/j.apsusc.2020.147781.

[18] N. Ikarashi, Atomic structure of a Ni diffused Si (001) surface layer: precursor to formation of NiSi$_2$ at low temperature, J. Appl. Phys. 107 (2010), 033505, https://doi.org/10.1063/1.3294691.

[19] U. Falke, F. Fenske, S. Schulze, M. Hietschold, XTEM studies of nickel silicide growth on Si(100) using a Ni/Ti bilayer system, Phys. Status Solidi A 162 (1997) 615–621, https://doi.org/10.1002/1521-396X(199708)162.

[20] P.A. Bennett, Z. He, D.J. Smith, F.M. Ross, Endotaxial silicide nanowires: a review, Thin Solid Films 519 (2011) 8434–8440, https://doi.org/10.1016/j.tsf.2011.05.034.

[21] G. Kellermann, L.A. Montoro, L.J. Giovanetti, P.C.S. Claro, L. Zhang, A.J. Ramirez, F.G. Requejo, A.F. Craievich, Formation of an extended CoSi$_2$ thin nanohexagons array coherently buried in silicon single crystal, Appl. Phys. Lett. 100 (2012), 063116, https://doi.org/10.1063/1.3683493.

[22] G. Kellermann, L.A. Montoro, L.J. Giovanetti, P.C.S. Claro, L. Zhang, A.J. Ramirez, F.G. Requejo, A.F. Craievich, Controlled growth of extended arrays of CoSi$_2$ hexagonal nanoplatelets buried in Si(001), Si(011) and Si(111) wafers, Phys. Chem. Chem. Phys. 17 (2015) 4945–4951, https://doi.org/10.1039/C4CP04738A.

[23] D.S. Costa, C. Huck-Iriart, G. Kellermann, L.J. Giovanetti, A.F. Craievich, F.G. Requejo, *In situ* study of the endotaxial growth of hexagonal CoSi$_2$ nanoplatelets in Si(001), Appl. Phys. Lett. 107 (2015), 223101, https://doi.org/10.1063/1.4936377.

[24] A.P. Peter, J. Meersschaut, O. Richard, A. Moussa, J. Steenbergen, M. Schaekers, Z. Tokei, S.V. Elshocht, C. Adelmann, Phase formation and morphology of nickel silicide thin films synthesized by catalyzed chemical vapor reaction of nickel with silane, Chem. Mater. 27 (2015) 245–254, https://doi.org/10.1021/cm503810p.

[25] J.P. Sullivan, R.T Tung, F. Schrey, Control of interfacial morphology: NiSi$_2$/Si (100), J. Appl. Phys. 72 (1992) 478, https://doi.org/10.1063/1.351878.

[26] L. Klein, M. Aparicio, A. Jitianu, Handbook of Sol-Gel Science and Technology, Springer, 2018, https://doi.org/10.1007/978-3-319-32101-1.

[27] A.M. Buckley, M. Greenblatt, The sol-gel preparation of silica gels, J. Chem. Educ. 71 (1994) 599, https://doi.org/10.1021/ed071p599.

[28] S. Sakka, Formation of particles in sol-gel process, KONA 7 (1989) 106–118, https://doi.org/10.14356/kona.1989017.

[29] S.M. Attia, J. Wang, G. Wu, J. Shen, J. Ma, Review on sol-gel derived coatings: process, techniques and optical applications, J. Matter. Sci. Technol. 18 (2002) 211–218.

[30] M. Tolan, X-ray Scattering from Soft-Matter Thin films. Springer-Verlag, Springer, Berlin, Heidelberg, 1999.

[31] J.J. Fuentes-Gallego, E. Blanco, L. Esquivias, Ellipsometric characterization of an AISI 304 stainless steel protective coating, Thin Solid Films 301 (1997) 12–16, https://doi.org/10.1016/S0040-6090(97)00013-8.

[32] M.G. Wardle, J.P. Goss, P.R. Briddon, R. Jones, Structural and electronic properties of thin fluorite-structure NiSi$_2$, CoSi$_2$ and FeSi$_2$ interfaces and precipitates in Si, Phys. Status Solidi A 202 (2005) 883–888, https://doi.org/10.1002/pssa.200460508.

[33] L.H. Wu, C.J. Tsaiz, Surface cleanness dependence of the Interfacial orientation of endotaxial NiSi$_2$ on Si(001), Electrochem. Solid State Lett. 12 (2008) H73–H76, https://doi.org/10.1149/1.3058995.

[34] N. Mingo, D. Hauser, N.P. Kobayashi, M. Plissonnier, A. Shakouri, Nanoparticle-in-alloy approach to efficient thermoelectrics: silicides in SiGe, Nano Lett. 9 (2009) 711–715, https://doi.org/10.1021/nl8031982.

[35] N. Uchida, T. Tada, Y. Ohishi, Y. Miyazaki, K. Kurosaki, S. Yamanaka, Heavily doped silicon and nickel silicide nanocrystal composite films with enhanced thermoelectric efficiency, J. Appl. Phys. 114 (2013), 134311, https://doi.org/10.1063/1.4823814.

[36] R. Guo, B. Huang, Approaching the alloy limit of thermal conductivity in single-crystalline Si-based thermoelectric nanocomposites: a molecular dynamics investigation, Sci. Rep. 5 (2015), https://doi.org/10.1038/srep09579.